Assessment of Friction Upscaling Methods in Dual-Mesh Shallow Water Simulations

Alireza Shamkhalchian[1], Gustavo A. M. de Almeida[2], and Ricardo Mantilla[3]

[1]Postdoctoral research fellow, Department of Civil Engineering, Price Faculty of Engineering, University of Manitoba, Manitoba, Canada. Email: Alireza.Shamkhalchian@umanitoba.ca (Corresponding author)

[2]Associate Professor, Faculty of Engineering and Physical Sciences, University of Southampton, Southampton, Hampshire, UK. Email: G.deAlmeida@soton.ac.uk

[3]Associate Professor, Department of Civil Engineering, Price Faculty of Engineering, University of Manitoba, Manitoba, Canada. Email: Ricardo.Mantilla@umanitoba.ca

ABSTRACT

This study investigates the challenge of accurately upscaling the friction source term of the 2D Shallow Water Equations in computational simulations using nested meshes (also known as dual-meshes) for large-scale flood inundation problems. This work employs a recently developed dual-meshes sub-grid (SG) model, which performs runtime computations on a coarse computational mesh while incorporating high resolution information from a fine mesh at the pre-processing stage. Four approaches proposed in the literature to approximate the friction source term are compared. They are formulated based on assumptions such as constant friction slope and constant water depth over a computational cell. The models are evaluated using two 1D idealized test cases covering a wide range of flow regimes, water depths, and discharges, and two large-scale 2D real-world test cases. Methods that upscale the solution to compute frictional effects on a coarse-resolution mesh deliver 2-5x speedup relative to approaches performing friction computations on a fine-scale mesh. However, the speedup varies depending on the specific case. The approach delivering the

best trade-off between accuracy and computational performance upscales friction by assuming a constant flow direction over each coarse cell. A detailed discussion is provided on the impact of various assumptions in the approximation of the friction source term on solution accuracy, and the limitations of the approach are explained.

PRACTICAL APPLICATIONS

The numerical solution of the two-dimensional shallow water equations is an essential tool in flood risk management. However, obtaining accurate solutions using conventional methods typically requires finely resolved computational meshes, which often translates into computing times that are prohibitively long. This paper deals with dual-mesh methods to improve the accuracy of coarse-grid simulations, leading to fast flood inundation models. These methods incorporate important topographic and roughness features, while the main computations are performed at coarse resolution. In this paper we show that the specific way they include these features into the computations, and in particular, into friction estimations, plays an important role in the solutions. The paper presents a detailed assessment of methods recently proposed to model friction in dual-mesh models, linking the results of our tests to key assumptions adopted in each case. The findings provide insights into the strengths and limitations of each method and will guide practitioners in choosing appropriate approaches for reliable and efficient flood modeling in real-world scenarios involving multi-resolution grids.

INTRODUCTION

Computational simulation of flood inundation has evolved through the last decades to become a vital tool supporting flood risk assessment, emergency response, and engineering design. Solutions to such problems often require the analysis of numerous scenarios through multiple runs of numerical models. Approaches developed by industry and research institutions that leverage numerical solutions of the shallow water equations (SWE) are particularly relevant to these tasks, as they incorporate terrain and land cover data to provide realistic computational simulations (e.g., Alcrudo and García-Navarro 1993, Guinot and Soares-Frazão 2006, Toro and Garcia-Navarro 2007,

Sanders et al. 2008,Kesserwani and Liang 2015, Shaw and Kesserwani 2020, Xing et al. 2022, Kesserwani and Sharifian 2023, Horváth et al. 2020, and Qi et al. 2024 among many others). However, incorporating high-resolution data into large-scale flood models is crucial but challenging, as it significantly increases computational demands. This dilemma has motivated research on developing efficient models that can support real-time urban flood forecasting, catchment-wide analyses, and interactive risk communication tools (Sanders and Schubert 2019; Dewals et al. 2021). Although recent advancements have improved computational efficiency, current models still fall short of the performance needed for large-scale, detailed flood simulations essential for decision-making (Wijaya et al. 2023).

Extensive research has been devoted to the development of modeling techniques that balance computational speed and accuracy. These techniques include parallel computing (e.g., Neal et al. 2009; Kesserwani and Sharifian 2023), adaptive meshes (e.g., Rogers et al. 2001; Kirstetter et al. 2021), coupled 1D–2D models (e.g., Morales-Hernández et al. 2016; Kang and Kubatko 2024), simplified SWE models (e.g., Horritt and Bates 2001; Wang et al. 2011), and more recently also solutions leaveraging machine-learning techniques (e.g., Qi et al. 2024; Yin et al. 2025) to name only a few. One interesting alternative involves using sub-grid parameterizations within the governing equations, offering flexibility to complement other techniques. This strategy aims to approximate some physical processes operating within a large computational cell (e.g. influenced by sub-grid scale topography) without performing high-resolution computations, thereby improving simulation accuracy at lower resolutions. Given that explicit numerical schemes for solving 2D SWE are highly sensitive to grid resolution [typically, $C \sim \Delta x^{-3}$, where C is the computational cost and Δx the grid size], grid coarsening can significantly enhance model performance. However, coarsening the grid may compromise numerical accuracy due to increased truncation errors, by misrepresenting topographical features crucial for flood propagation (Begnudelli et al. 2008; Yu and Lane 2006).

Since its initial proposal by Defina et al. 1994, sub-grid models have largely focused on concept porosity to model the effects of sub-grid topography on the storage within cells and momentum fluxes across its edges (Sanders et al. 2008; Soares-Frazão et al. 2008; Guinot et al. 2017). More

recently, nested-mesh models have gained attention (Volp et al. 2013; Hénonin et al. 2015; Sanders and Schubert 2019; Shamkhalchian and de Almeida 2021; Shamkhalchian and de Almeida 2023). These models use a coarse mesh as a base, with a high-resolution mesh nested within to integrate fine-scale topography and roughness data. They are defined to offer a dynamic interpretation —dependent on water surface elevation— of cell volume and edge length contributions to storage and conveyance. Additionally, the high-resolution data aids in approximating the friction and bed slope source terms in the SWEs. Sub-grid models utilizing low-resolution computational meshes are designed to mitigate errors typically associated with grid coarsening by incorporating high-resolution data. However, these models are limited in addressing the loss of accuracy in problems involving steep gradients or discontinuities in the solution.

Specific approaches proposed in the literature to represent the physics operating at small scale to coarse cells (i.e. upscaling), as well as the numerical methods employed, vary significantly across models. For example, Volp et al. 2013 used the Finite Volume (FV) method to solve SWEs, upscaling depths and velocities by spatially averaging variables over the wet portion of coarse cells, assuming constant friction slope and uniform flow direction. In contrast, Hénonin et al. 2015 averaged water depths similarly but assumed a piecewise constant free surface elevation, using the ADI Finite Difference scheme. Sanders and Schubert 2019 applied the Finite Volume method, averaging water depth and unit width discharge over wet cell portions and computing fluxes along coarse cell edges at fine resolution using downscaled depths and local topography. The models by Shamkhalchian and de Almeida 2021 and Shamkhalchian and de Almeida 2023 adopted a similar approach, computing fluxes along coarse edges at fine resolution while solving the Riemann problem with downscaled depths and velocities. In Shamkhalchian and de Almeida 2021 and Shamkhalchian and de Almeida 2023, the friction upscaling method was defined by first analytically integrating the flow resistance equation over coarse cells under the assumption of a constant flow direction across the cell. Further details about the approaches above can be found in the respective articles, while specific information relevant to this paper is provided in the following sections.

The fundamentally different approaches proposed in the literature to upscale friction in nested-mesh models raises the question of how the underlying assumptions of each method impact solution accuracy. Answering this question is crucial for guiding researchers and model developers in selecting appropriate friction models, by recognizing their limitations, and may also prompt future development of improved models to address existing limitations. The aim of this paper is to comparatively examine various friction approximation techniques that have been proposed for nested-mesh models.

To enable a rigorous comparison of solutions, friction models were implemented within the same SG model, ensuring that the solution methods for the homogeneous SWEs and bed slope terms remain consistent, with friction models as the only variable. The models are tested in both idealized and real-world scenarios, and the paper provides technical discussions on the results, especially regarding the constant friction slope assumption within a cell.

The paper is organized as follows: the first section introduces the governing equations and numerical methods used by the SG model, detailing its treatment of all terms except the friction source term. This is followed by a section describing the various approaches previously proposed for upscaling the friction source term in nested-mesh models. In the third section, friction approximation methods are tested using both real-world and artificial cases. The last section synthesizes the study's main insights and conclusions.

THE SG MODEL CONSTRUCTION

This section outlines the SG model used in this paper to solve the governing equations. A comprehensive description of the model can be found in Shamkhalchian and de Almeida 2021, and Shamkhalchian and de Almeida 2023.

Governing Equations and Structured Meshes

The SG model predicts water surface level and unit width discharge in time and space by solving the integral form of the 2D shallow water equations at computational cells with area Ω boundary

Γ, respectively:

$$\frac{\partial}{\partial t}\int_{\Omega}\mathbf{U}\mathrm{d}\Omega+\oint_{\Gamma}[\mathrm{E}(\mathbf{U})\cdot\mathbf{e}]\mathrm{d}\Gamma=\int_{\Omega}\mathbf{S}(\mathbf{U})\mathrm{d}\Omega, \tag{1}$$

where,

$$\mathbf{U}=\begin{bmatrix}\eta\\ q_x\\ q_y\end{bmatrix},\quad \mathrm{E}=[\mathbf{F},\mathbf{G}],\quad \mathbf{F}(\mathbf{U})=\begin{bmatrix}q_x\\ \frac{q_x^2}{h}+\frac{g}{2}h^2\\ \frac{q_xq_y}{h}\end{bmatrix},\quad \mathbf{G}(\mathbf{U})=\begin{bmatrix}q_y\\ \frac{q_xq_y}{h}\\ \frac{q_y^2}{h}+\frac{g}{2}h^2\end{bmatrix}, \tag{2}$$

$$\mathbf{S}(\mathbf{U})=\mathbf{S}_b(\mathbf{U})+\mathbf{S}_r(\mathbf{U}),\quad \mathbf{S}_b(\mathbf{U})=\begin{bmatrix}0\\ ghS_{0_x}\\ ghS_{0_y}\end{bmatrix},\quad \mathbf{S}_r(\mathbf{U})=\begin{bmatrix}0\\ -ghS_{f_x}\\ -ghS_{f_y}\end{bmatrix}, \tag{3}$$

t denotes time, $\mathbf{e}=[e_x,e_y]$ is the outward unit vector normal to the boundary Γ, Ω denotes the area of the subdomain of integration, η denotes water surface elevation, h is water depth and g represents the gravitational acceleration, $\mathbf{q}=\left[q_x,q_y\right]^{\mathrm{T}}$ is the unit width discharge vector, $\mathbf{S}_0=\left[S_{0x},S_{0y}\right]^{\mathrm{T}}$ and $\mathbf{S}_f=\left[S_{fx},S_{fy}\right]^{\mathrm{T}}$ are the bed and friction gradients, respectively. Friction is modeled using Manning's equation, i.e., $\mathbf{S}_f=\frac{\mathbf{q}\|\mathbf{V}\|n_M^2}{h^{7/3}}$, $\|V\|=\sqrt{u^2+v^2}$, where u and v are the x and y components of the velocity vector of magnitude $\|\mathbf{V}\|$. The conserved variable h in the vector $\mathbf{U}(x,y,t)$ is replaced with η to enable the model to reconstruct the water surface elevation as piecewise constant or piecewise linear, as required as part of the FV solution described next. The water depth is then distributed as $h=\eta-z$ assuming a non-erodible bed (i.e., $\frac{\partial z}{\partial t}=0$).

The computational domain of the SG model is defined as a rectangular region that is discretized by two sets of nested Cartesian meshes, as depicted in Fig. 1. The low-resolution mesh (also referred to as the "coarse mesh" or "computational mesh") is employed to solve the governing equations, while the high-resolution mesh (the "fine mesh") contains detailed topographic and roughness data. Information such as velocity, depth, bed elevation, and roughness at the fine resolution is defined as a piecewise constant within each small cell. The high-resolution data is used to improve the accuracy of the solutions by applying upscaling methods, as explained in the

following sections. These methods aim to reduce errors that typically occur when computations are performed at coarse resolution by ensuring that fine-scale information is accounted within the coarse-resolution model, thus maintaining computational efficiency and accuracy.

The x and y axes are defined along the horizontal and the vertical coordinates of the domain, the dimensions of which along the same axes are L_d and W_d, as shown in Fig. 1. The dimensions of large and small cells in the x and y directions are denoted by $\Delta x, \Delta y$ and δx, δy, respectively. Each large cell consists of four edges Γ_1 to Γ_4 labeled anticlockwisely as shown in Fig. 1. Large cells are indexed by i ranging from 1 to N, where N corresponds to the total number of large cells within the study domain (i.e.$N = \frac{W_d L_d}{\Delta x \Delta y}$). Within each large cell, the indices j and k are used to define the position of small cells within large cells along the x and y directions, respectively. The values of j and k satisfy $1 \leq j \leq J$ and $1 \leq k \leq K$, where $J = \frac{\Delta x}{\delta x}$ and $K = \frac{\Delta y}{\delta y}$. As an example, $z_i \mid_{j,k}$ denotes the bed elevation at the j^{th} column and k^{th} row of small cells within the i^{th} large cell.

SG Model Solution Process

The methodology used by the model to upscale each term in the governing equations from fine to coarse resolution is comprehensively explained in Shamkhalchian 2021, Shamkhalchian and de Almeida 2021 and Shamkhalchian and de Almeida 2023. In this paper, only a concise overview of the process is presented. The model upscales the equations through integration over the coarse-resolution cell. While the quantities vary within a large cell of the SG model, their integrated form is denoted by the overbar symbol. For example, the upscaled vector of these variables is defined as

$$\overline{\mathbf{U}} = \frac{1}{\Omega} \int_{\Omega} \mathbf{U} \mathrm{d}\Omega, \tag{4}$$

The tilde symbol is used to define quantities averaged over the wet portion of the area (i.e., Ω_w), i.e.:

$$\tilde{\mathbf{U}} = \frac{1}{\Omega_w} \int_{\Omega_w} \mathbf{U} \mathrm{d}\Omega = \frac{1}{r} \overline{\mathbf{U}}, \tag{5}$$

where, $r = \frac{\Omega_w}{\Omega}$. As an example, consider the unit-width discharge:

$$\overline{\mathbf{q}} = \frac{\int_{\Omega} \mathbf{q} \mathrm{d}\Omega}{\Omega} = \frac{\int_{\Omega_w} \mathbf{q} \mathrm{d}\Omega + \int_{\Omega_d} 0 \, \mathrm{d}\Omega}{\Omega} = \tilde{\mathbf{q}} \frac{\Omega_w}{\Omega} = \tilde{\mathbf{q}} r, \tag{6}$$

where Ω_d represents the dry fraction of a computational cell.

Time integration is performed by advancing the solution from time level n to $n+1$ using a time step Δt through a fractional step (e.g., Lions and Mercier 1979; LeVeque 2002; Toro 2013), whereby the solution is first computed at an intermediate state denoted by *. In the first operation, the solution is updated for all terms of the governing equations, except for the bed resistance source term $\mathbf{S}_r$, to prevent numerical instabilities (Liang and Marche 2009). This is done using a first-order (in time) Euler method:

$$\overline{\mathbf{U}}_i^* = \overline{\mathbf{U}}_i^n - \frac{\Delta t}{\Omega_i} \sum_{(p,q) \in D_i} |\Gamma_{pq}| \mathrm{E}'(\mathbf{U}_p^n, \mathbf{U}_q^n, \mathbf{e}_{pq}) + \Delta t \overline{\mathbf{S}}_{b_i}^n, \tag{7}$$

where D_i is the set of indices referred to small neighboring cells p sharing a side with a small cell q contained within the large cell i ($\Omega_p \subset \Omega_i$ and $\Omega_q \not\subset \Omega_i$), $|\Gamma_{pq}|$ is the length of the edge between cells p and q (i.e. δx or δy), E' is the numerical flux vector, and $\mathbf{e}_{pq}$ is the unit outward vector. The time step Δt is dynamically computed using the Courant–Friedrichs–Lewy (CFL) condition (e.g., LeVeque 2002; Shamkhalchian 2021; Toro 2001). $\overline{\mathbf{S}}_{b_i}^n$ is defined as

$$\overline{\mathbf{S}}_{b_i}^n = \begin{bmatrix} 0 \\ \overline{S}_{b_x} \\ \overline{S}_{b_y} \end{bmatrix}_i^n \tag{8}$$

This term is approximated at the level of small cells and then extended to cover the larger cells, with the specific treatment of the SG model detailed in the subsequent sections.

The solution at time level $n+1$ is then obtained by adding the effect of frictional forces $\mathbf{S}_r$ through a semi-implicit method (Liang and Marche 2009; de Almeida et al. 2018; Sanders and

Schubert 2019). This is achieved by solving the following equation, which constitutes the focus of investigation in this study:

$$\frac{\mathrm{d}}{\mathrm{d}t}\int_{\Omega_i}\mathbf{U}\mathrm{d}\Omega = \int_{\Omega_i}\mathbf{S}_r\mathrm{d}\Omega, \tag{9}$$

which is numerically approximated as:

$$\overline{\mathbf{U}}_i^{n+1} = \overline{\mathbf{U}}_i^{*} + \Delta t\overline{\mathbf{S}}_{r_i}. \tag{10}$$

In Eq. (7), the mass and momentum fluxes are approximated by solving the Riemann problem using the method adapted for the SG model, as detailed in the following sections. This method solves the Riemann problem at the high-resolution mesh and then integrates the computed fluxes along each edge of large cells. The Riemann solver of Harten, Lax, and van Leer Contact (HLLC) developed by Toro et al. 1994 (e.g., Erduran et al. 2002; Kong 2011) is used by the SG model.

Flux Computations

The SG model implements a first-order accurate solution in time and includes both first-order (Shamkhalchian and de Almeida 2021) and second-order (Shamkhalchian and de Almeida 2023) spatial accuracy solutions. In this work, the second-order accurate model is used. To achieve the second-order spatial accuracy akin to conventional FV models, the three components of $\overline{\mathbf{U}}_i^n$ (i.e., water surface level and unit width discharges in the x and y directions) within coarse cells are defined using a piecewise linear reconstruction of variables. To ensure numerical stability, (i) the slope of the piecewise linearization is constrained using the minmod method (LeVeque 2002) and (ii) at the wet-dry front the spatial order of accuracy is reduced to first order. Specifically, when a fully- or partially-wet large cell approaches a fully-dry cell, the reconstruction of variables is piecewise constant.

Dual-mesh models typically use information at fine-resolution to improve the accuracy of computations. One crucial step of such an approach is the specific method used to downscale the averaged values of $\overline{\mathbf{U}}_i^n$ along the edges of large cells. The SG model downscales the flow depth by assuming a constant free surface $\eta_i^n\,|_{\Gamma_m}$, which implies that $h_i^n\,|_{\Gamma_m} = \max(\eta_i^n\,|_{\Gamma_m} - z_i\,|_{\Gamma_m}, 0)$ along

the edge varies according to the bed elevations only (see Fig. 2). The other two components of $\overline{\mathbf{U}}_i^n$ (i.e. q_x, q_y) are downscaled under the assumption of a constant friction slope, which is also modeled using Manning's expression (Chow 1959; Cunge et al. 1980; Burguete et al. 2007; Viero and Valipour 2017). The procedure used to downscale the x-component of unit width discharge $q_{x_i}^n\,|_{\Gamma_m}$ is illustrated here as an example (the same approach is used for the y-component $q_{y_i}^n\,|_{\Gamma_m}$ and the other edges Γ_1 to Γ_3), as follows (refer to Fig. 2 for further details):

$$q_{x_i}^n\,\big|_{1,k} = \left[\frac{\left(\frac{1}{n_M}h^{\frac{5}{3}}\right)_{1,k}}{\left[(\eta-\tilde{z})^{\frac{5}{3}}\,T_1+\frac{5}{3}\,(\eta-\tilde{z})^{\frac{2}{3}}\,T_2+\frac{5}{9}\,(\eta-\tilde{z})^{\frac{-1}{3}}\,T_3\right]_{\Gamma_4}}\right]_i^n \overline{q}_{x_i}^n, \qquad 1\le k\le N_{\Gamma_4}^n, \tag{11}$$

where, $q_{x_i}^n\,|_{1,k}$ denotes the x-component of unit width discharge at time level n and for the kth small cell, $N_{\Gamma_4}^n$ is the number of submerged small cells adjacent to edge Γ_4 (which may vary in time if the large cell is partially wet), $\tilde{z}_i^n\,|_{\Gamma_4}$ represents the average bed level of submerged small cells in the vicinity of Γ_4 at the ith large cell and at time level n . The variables $T_{1_i}^n\big|_{\Gamma_4}$, $T_{2_i}^n\big|_{\Gamma_4}$,and $T_{3_i}^n\big|_{\Gamma_4}$ are defined (Shamkhalchian and de Almeida 2021) as follows:

$$T_{d_i}^n\big|_{\Gamma_4} = \left\{\frac{1}{N_{\Gamma_4}}\sum_{k=1}^{N_{\Gamma_4}}\left[\frac{\left(\tilde{z}|_{\Gamma_4}-z\right)^{(d-1)}}{n_M}\right]_{1,k}\right\}_i^n, d=1,2,3. \tag{12}$$

The downscaled values of $\mathbf{U}$ along both sides of the edges of large cells define the fine-resolution Riemann problem, which is solved by the HLLC solver. Integration of these fluxes along each edge of large cells yields the overall flux, which is subsequently used in Eq. (7).

Bed Slope Source Term

The bed slope source term is approximated in the model by an approach similar to that proposed by Valiani and Begnudelli 2006, which was adapted in Shamkhalchian and de Almeida 2021 for the SG model. The method assumes a constant water surface elevation η within each large cell, which yields an expression that is a function of η and the bed elevations near the edges of computational cells. That is, the topography between edges (or between an edge and a wet-dry front in the case

of partially wet cells) does not influence the bed slope approximation. For the sake of brevity, we present the discretization of the x-component of S_b only (refer to Shamkhalchian 2021 and Shamkhalchian and de Almeida 2021 for the complete derivation):

$$\overline{S}^{n}_{b_{x_i}} = \frac{g}{\Delta x K} \sum_{k=1}^{K} \left\{ \left(\acute{z} \mid_{1,k} - \acute{z} \mid_{J,k} \right) \left[\eta - \frac{1}{2} \left(\acute{z} \mid_{1,k} + \acute{z} \mid_{J,k} \right) \right] \right\}^{n}_{i}, \tag{13}$$

where $K = \Delta y / \delta y$ represents the number of rows of the small cells in the large cell, and $\acute{z}(z, \eta)$, defined as $\acute{z}(z, \eta) = \min(z, \eta)$, ensures that in partially wet cells, negative water depths do not occur in dry areas when calculating the term $h = \eta - z$ to approximate the integral of Eq. (13).

ALTERNATIVE METHODS TO UPSCALE THE FRICTION TERM

This section describes the different approaches that have been proposed in the literature to approximate the friction term [i.e. Eq. (9)], which will later be compared in this paper. Since the first component of the vector $\mathbf{S}_r$ is zero-valued by definition, the problem of updating the solution to account for friction is reduced to

$$\frac{\mathrm{d}}{\mathrm{d}t}\mathbf{q} = -gh\mathbf{S}_f\left(\mathbf{U}\right), \tag{14}$$

which can be integrated over the area of a large cell to advance the solution from the initial condition $\mathbf{q}^*$ to time level $n+1$ through:

$$\frac{\mathrm{d}}{\mathrm{d}t}\int_{\Omega_i} \mathbf{q}\mathrm{d}\Omega = \int_{\Omega_i} -gh\mathbf{S}_f \mathrm{d}\Omega. \tag{15}$$

Several discretization techniques have been proposed in the literature to integrate this source term, including explicit, implicit, and semi-implicit schemes. In this paper, all friction approaches are based on a widely-used semi-implicit technique (e.g., Liang and Marche 2009; Kesserwani and Liang 2012; Cea and Bladé 2015; de Almeida et al. 2018; Sanders and Schubert 2019). This choice is supported by its successful application to a wide range of flood inundation problems, as well as

its time efficiency, where

$$\mathbf{S}_f = \frac{\mathbf{q}^{n+1} \parallel \mathbf{q}^* \parallel}{\left(\frac{h^{\frac{10}{3}}}{n_M^2}\right)^*}. \tag{16}$$

In dual mesh models, within a computational cell (i.e., at the level of small cells), variables are distributed, and their upscaled quantities replace the corresponding variables in Eq. (16). The upscaling procedure is not unique and depends on the adopted set of assumptions, which are detailed in the following sections. Across all the upscaling techniques discussed, a common assumption is that the water surface elevation, η_i, remains constant across large cells.

Friction solution based on cell-averaged (AVG) values of variables

The first approach to approximating Eq. (15) involves substituting values of variables that are averaged over the wet part of large cells. This method is hereafter referred to as AVG and formulated based on the assumptions utilized in the work of Hénonin et al. 2015. The method accounts for partially-wet cells by defining variables integrated over the wet portion of partially-wet cells. Discretizing Eq. (15) for the wet portion of a cell, by applying a first-order forward finite difference to the LHS and using averaged variable values on the RHS in combination with Eq. (16), yields:

$$\frac{\tilde{\mathbf{q}}_i^{n+1} - \tilde{\mathbf{q}}_i^*}{\Delta t} = -g \frac{\tilde{\mathbf{q}}_i^{n+1} \parallel \tilde{\mathbf{q}}_i^* \parallel}{\frac{(\eta - \tilde{z})^{\frac{7}{3}}}{\tilde{n}_M^2}} \tag{17}$$

Including Eq. (6), i.e., $\overline{\mathbf{q}} = \tilde{\mathbf{q}} r$ gives:

$$\overline{\mathbf{q}}_i^{n+1} = \left[\frac{\overline{\mathbf{q}}}{1 + \frac{g \|\overline{\mathbf{q}}\| \Delta t}{r\left(\frac{(\eta - \tilde{z})^{\frac{7}{3}}}{\tilde{n}_M^2}\right)}} \right]_i^*. \tag{18}$$

The main advantage of this approach is that expensive fine-scale computations of averaged values can be performed at pre-processing, thus incurring no additional runtime cost.

The constant friction slope (CFS) approach

A popular method adopted to upscale the effects of friction over a large region of the domain (e.g. the computational cell) is to assume a constant value of the friction slope (e.g., Volp et al. 2013; Sanders and Schubert 2019). The particular approach described here is similar to that used by Sanders and Schubert 2019, which in addition also assumes a constant value of $\mathbf{q}$ over the large computational cell, $\left(\mathbf{q}_{j,k}\right)_i = \tilde{\mathbf{q}}_i$. The RHS of Eq. (15) equals $-g\,\widetilde{h\mathbf{S}_f}$. In this method, the term $\widetilde{h\mathbf{S}_f}$ is approximated by the product of the averaged variables, i.e., $\widetilde{h\mathbf{S}_f} \approx \tilde{h}\,\tilde{\mathbf{S}}_f$. Using Eq. (16), and under the assumption that $\widetilde{\frac{1}{\left(\frac{h^{\frac{5}{3}}}{n_M}\right)^2}} = \frac{1}{\widetilde{\left(\frac{h^{\frac{5}{3}}}{n_M}\right)^2}}$,

$$\tilde{S}_f = \frac{\tilde{\mathbf{q}} \| \tilde{\mathbf{q}} \|}{\widetilde{\left(\frac{h^{5/3}}{n_M}\right)^2}}, \tag{19}$$

where,

$$\widetilde{\left(\frac{h^{5/3}}{n_M}\right)} = \frac{1}{\Omega_{w_i}} \int_{\Omega_{w_i}} \left(\frac{h^{5/3}}{n_M}\right)^* \mathrm{d}\Omega_w \simeq \left[\frac{1}{N_w} \sum_{j=1}^{J} \sum_{k=1}^{K} \left(\frac{h^{5/3}}{n_M}\right)_{j,k}\right]_i^*, \tag{20}$$

where N_w is the number of wet small cells in the large cell i. Using Eq. (19), Eq. (6), and the same approach as described for the AVG method, yields:

$$\overline{\mathbf{q}}_i^{n+1} = \left[\frac{\overline{\mathbf{q}}}{1 + \frac{g(\eta - \tilde{z})\|\overline{\mathbf{q}}\|\Delta t}{r^2 \widetilde{\left(\frac{(\eta-z)^{\frac{5}{3}}}{n_M}\right)^2}}}\right]_i^*. \tag{21}$$

The term $\widetilde{\left(\frac{h^{5/3}}{n_M}\right)}$ in Eq. (19) is used to approximate the aggregated effects of variable topography on the frictional force. Values of this term (which require fine-resolution computations) can be obtained at pre-processing time and stored in lookup tables. Conceptually, the assumption of constant values for η and $\mathbf{q}$ over a bed with non-uniform elevations implies that velocities increase in shallow flow regions (tending to infinity as the depth tends to zero). This assumption contradicts the typical characteristics of flow observed in open channels.

The Friction Model Based on the Parallel Flow (PF) Distribution Assumption

Shamkhalchian and de Almeida 2021 proposed an alternative method to upscale the effect of friction over large computational cells where the velocity, topography and roughness are non-uniform. The approach does not assume constant values of any of the variables involved, and instead, only assumes that the velocity vectors within the large cell are parallel (which in many scenarios may be a more realistic approximation). The following paragraphs provide a detailed description of the approach. First, by combining Eqs. (14) and (16), yields:

$$\frac{\mathrm{d}}{\mathrm{d}t}\left(\mathbf{q}_{j,k}\right)_i = \left\{-g\left[\frac{n_M^2\mathbf{q}^{n+1}\parallel\mathbf{q}^*\parallel}{(h^*)^{\frac{7}{3}}}\right]_{j,k}\right\}_i. \tag{22}$$

The central premise of this upscaling approach rests on the assumption that, across a large cell, the flow direction remains constant, although the magnitudes may vary. Thus, $\mathbf{q}_{j,k}(x,y)|_i = \left[\varphi_{j,k}(x,y)\,\tilde{\mathbf{q}}\right]_i$, where $\varphi_i(x,y)$ is a scalar function representing the distribution of unit width discharge within the large cell. This interpretation transforms Eq. (22) into the form:

$$\frac{\mathrm{d}}{\mathrm{d}t}\left(\varphi_{j,k}\tilde{\mathbf{q}}\right)_i = \left\{-g\tilde{\mathbf{q}}^{n+1}\parallel\tilde{\mathbf{q}}^*\parallel\left[\frac{\varphi^*\varphi^{n+1}n_M^2}{(h^*)^{\frac{7}{3}}}\right]_{j,k}\right\}_i. \tag{23}$$

In addition, we assume that the flow distribution [thus, the function $\varphi_i(x,y)$] remains time-independent during each time step (therefore also from the intermediate state * to $n+1$), i.e., $\left(\varphi_{j,k}^*\right)_i \approx \left(\varphi_{j,k}^{n+1}\right)_i$ or $\frac{\mathrm{d}}{\mathrm{d}t}\left(\varphi_{j,k}\right)_i \cong 0$. This assumption readily leads to the inference that $\left(\tilde{\mathbf{q}}\frac{\mathrm{d}}{\mathrm{d}t}\varphi_{j,k}\right)_i \ll \left(\varphi_{j,k}\frac{\mathrm{d}\tilde{\mathbf{q}}}{\mathrm{d}t}\right)_i$ yielding:

$$\left[\frac{(h^*)^{\frac{7}{3}}}{n_M^2}\right]_{(j,k)_i}\frac{\mathrm{d}}{\mathrm{d}t}\tilde{\mathbf{q}}_i = \left[-g\tilde{\mathbf{q}}^{n+1}\parallel\tilde{\mathbf{q}}^*\parallel\varphi_{j,k}^{n+1}\right]_i. \tag{24}$$

Integrating Eq. (24) over the wet region of the large cell and considering that $\tilde{\mathbf{q}}^*$ and $\tilde{\mathbf{q}}^{n+1}$ are constant within it, yields

$$\frac{\mathrm{d}}{\mathrm{d}t}\tilde{\mathbf{q}}_i\int_{\Omega_{w_i}}\left[\frac{(h^*)^{\frac{7}{3}}}{n_M^2}\right]_{j,k}\mathrm{d}\Omega_w = -g\tilde{\mathbf{q}}^{n+1}\parallel\tilde{\mathbf{q}}^*\parallel\int_{\Omega_{w_i}}\varphi_{j,k}^{n+1}\mathrm{d}\Omega_w. \tag{25}$$

However, since by definition $\tilde{\mathbf{q}}_i^{n+1} = \Omega_{w_i}^{-1} \int_{\Omega_{w_i}} \mathbf{q}_{j,k}^{n+1} \mathrm{d}\Omega_w = \Omega_{w_i}^{-1} \int_{\Omega_{w_i}} \varphi_{j,k}^{n+1} \tilde{\mathbf{q}}^{n+1} \mathrm{d}\Omega_w$, it follows that $\int_{\Omega_{w_i}} \varphi_{j,k}^{n+1} \mathrm{d}\Omega_w = \Omega_{w_i}$, and

$$\frac{\mathrm{d}}{\mathrm{d}t}\tilde{\mathbf{q}}_i = \left[\frac{-g\tilde{\mathbf{q}}^{n+1} \parallel \tilde{\mathbf{q}}^* \parallel}{\widetilde{\left(\frac{h^{\frac{7}{3}}}{n_M^2}\right)}^*} \right]_i, \tag{26}$$

where,

$$\widetilde{\left(\frac{h^{\frac{7}{3}}}{n_M^2}\right)}_i^* = \frac{1}{\Omega_{w_i}} \int_{\Omega_{w_i}} \left[\frac{(h^*)^{\frac{7}{3}}}{n_M^2} \right]_{j,k} \mathrm{d}\Omega_w \simeq \left[\frac{1}{N_w} \sum_{j=1}^{J} \sum_{k=1}^{K} \left(\frac{h^{\frac{7}{3}}}{n_M^2} \right)_{j,k} \right]_i^*. \tag{27}$$

Applying the same discretization approach as in the previous sections—namely, a first-order forward-time finite difference scheme for the derivative in Eq. (26), together with Eq. (6)—yields:

$$\overline{\mathbf{q}}_i^{n+1} = \left[\frac{\overline{\mathbf{q}}}{1 + \frac{g\|\overline{\mathbf{q}}\|\Delta t}{r\widetilde{\left(\frac{(\eta-z)^{\frac{7}{3}}}{n_M^2}\right)}}} \right]_i^* = \left[\frac{\overline{\mathbf{q}}}{1 + \frac{g\|\overline{\mathbf{q}}\|\Delta t}{r\widetilde{\left(\frac{h^{\frac{7}{3}}}{n_M^2}\right)}}} \right]_i^*. \tag{28}$$

Updating friction through Eq. (28) could significantly increase the computational load of the model during runtime, since Eq. (27) requires computations at fine resolution. To avoid this, Shamkhalchian 2021 and Shamkhalchian and de Almeida 2021 proposed an efficient approximation to Eq. (27), whereby the term $\left(h_i^*\right)_{j,k}^{\frac{7}{3}}$ is expressed using a Taylor series centered about $\tilde{h}_i^*$, while terms of order higher than two in the Taylor series are neglected. This methodology (for further details referrer to Shamkhalchian 2021) results in the following friction expression

$$\overline{\mathbf{q}}_i^{n+1} = \frac{\overline{\mathbf{q}}_i^*}{\sigma_i^*}, \qquad \sigma_i^* = \left[1 + \frac{1}{r} \frac{g \parallel \overline{\mathbf{q}} \parallel \Delta t}{(\eta - \tilde{z})^{\frac{7}{3}} T_4 + \frac{7}{3}(\eta - \tilde{z})^{\frac{4}{3}} T_5 + \frac{14}{9}(\eta - \tilde{z})^{\frac{1}{3}} T_6} \right]_i^*, \tag{29}$$

where

$$T_{d_i}^* = \left\{ \frac{1}{N_w} \sum_{j=1}^{J} \sum_{k=1}^{K} \left[\frac{(\tilde{z} - z)^{d-4}}{n_M^2} \right]_{j,k} \right\}_i^*, \quad d = 4, 5, 6. \tag{30}$$

The parameters T_4, T_5 and T_6 depend on roughness and topography only. They are pre-processed as a function of the number of submerged small cells, stored in a table, and are readily retrieved during runtime at negligible cost.

The friction model in this section (i.e., PF) offers two alternatives. The first, detailed in Eq. (28), involves updating $\overline{q}$ for friction at a high-resolution mesh, computed small cell by small cell. The second alternative, provided in Eq. (29), is an approximation of Eq. (28). These two alternatives are denoted as PFE and PFA, respectively wherein the "E" and "A" suffixes to PF stand for "Exact" and "Approximation".

APPLICATIONS AND RESULTS

In this section, a set of selected idealized and real-world test cases are used to compare the accuracy and computational efficiency of models built using each of the friction upscaling methods described in the previous section. These models are also compared against a high-resolution benchmark solution (BMS), which is obtained using a conventional (i.e., single-mesh) Godunov-type FV model that uses the HLLC Riemann solver to solve the 2D SWE over regular quadrilateral cells. This model is a specific case of the SG model for $\Delta x = \delta x$ and $\Delta y = \delta y$. The focus on the comparison against a fine-resolution model is justified by the very objective of upscaling, which is to provide an accurate approximation to such model. To ensure that the proposed models are well-balanced, various tests have been conducted to verify C-property compliance (see e.g., Bermudez and Vazquez 1994; Duran and Marche 2014). While these results are omitted here for brevity, they confirm that the models maintain stability and accuracy in line with well-balanced conditions.

Results presented in the following sections are labeled using the acronym of the friction upscaling method followed by the resolutions of the coarse and fine-resolution meshes. For instance, AVG (50/5) denotes the solution by the AVG model with a large cell resolution of 50 m and a small cell resolution of 5 m.

The performance of the friction models is evaluated using two 1D test cases and one large-scale real-world test case. An additional 2D real-world test case is presented and discussed in the supplemental material.

Test Case 1: Unsteady Non-Uniform Flow in a Prismatic Channel with an Undulated Bed

The first test case aims to assess the performance of the proposed upscaling friction techniques in solving problems involving conditions ranging from partially to fully wet computational cells and containing significant variations in the averaged water depth of computational cells during the simulation and along the channel. The test simulates unsteady flow in a 3000-meter-long, prismatic one-dimensional channel with a sinusoidal bed profile, defined by $z = 0.5 - 0.05\sin(\frac{\pi}{500}x) - 0.000166x$, and a Manning roughness coefficient of 0.05. The cross-section of the channel comprises a semi-circular main channel and two 8.5-m wide symmetrical floodplains, each exhibiting an average lateral bed slope of 16%, as illustrated in Fig. 3. The cross sections are bounded by vertical walls on each side. The boundary conditions (time series of flow discharges upstream and water levels downstream) are depicted in Fig. 4. The initial condition is derived from the output of a steady-state flow simulation using the flow characteristics at $t = 0$ s. A digital elevation model (DEM) with a resolution of 1 meter is utilized to represent this topography. All friction models are simulated at resolutions of 100/1, 200/1, and 300/1, and their performances are compared with benchmark solutions obtained by BMS (1).

Fig. 5 presents the water surface profiles produced by each of the models tested in this paper at t=2, 7, and 17 days, alongside the bed level profile. As expected, analysis indicates that the simple averaging approach of AVG exhibits the lowest accuracy across all resolutions, while other more sophisticated methods incorporating additional details of topography and roughness to upscale the friction source term yield more accurate results. To further examine errors, the Root Mean Square Errors (RMSE) of each η solution relative to the BMS at the center of computational cells was computed at specific time instants (t = 2, 5, 7, 9, and 13 days). Table 1 displays the range of RMSE for the adopted models at various resolutions. Results in Table 1 show that the most accurate simulations are achieved with PFE, followed by PFA, which offers comparable accuracy relative to PFE. CFS ranks third, while the AVG results show RMSEs one order of magnitude larger than those by PFE. Table 2 lists the runtimes of each model for simulating 17 days of flooding. The data indicates that the fastest model is AVG, closely followed by PFA and CFS, which have similar

runtimes to AVG. However, PFE is approximately three times slower than the other three models. Considering the trade-off between accuracy and speed, PFA emerges as the best-performing model.

Test Case 2: Steady Transcritical Flow Analysis in a 1D Rectangular Channel with a Varying Bed Profile

The second test case aims to assess how different friction models perform under various flow conditions. It involves a 1D prismatic rectangular channel with a steady transcritical flow (i.e., supercritical flow upstream and subcritical flow downstream) and a variable bed profile. It is important to note that the current generation of sub-grid models does not include methods to specifically model the transition from supercrititall (upstream) to subcritical flow (i.e. hydraulic jumps). Modelling such problems would require specific algorithms to infer the position of the hydraulic jump within the large cells. For this reason, such tests are not included in this and other papers on sub-grid models. This test case follows the inverse solution approach outlined by MacDonald 1996, where the channel's bed profile is derived from a predefined water depth profile for steady, non-uniform flow. The channel is 3000 m long and 10 m wide, with a uniform Manning's roughness coefficient of 0.025. A steady discharge of $Q = 100\ \mathrm{m^3 s^{-1}}$ is applied. The water depth follows the formula $h = 3 + 0.8 \sin\left(\frac{\pi}{2000}(x - 4000)\right)$, leading to spatially varying Froude numbers along the channel, as shown in Fig. 6. The inverse solution yields the corresponding bed profile, illustrated in Fig. 6. Simulations for this test case were carried out on computational grids with resolutions of 100 m, 200 m, 300 m, and a refined mesh of 1 m.

The numerical solutions for water surface elevation generated by each friction model at various resolutions are presented in Fig. 6. Overall, all models effectively replicate the analytical solutions. However, Table 3 offers a more comprehensive assessment of the models' accuracy by comparing the RMSE values of the solutions relative to the analytical solution at the center of the computational mesh. Consistent with the previous test case, PFE delivers the most accurate results, followed closely by PFA and CFS, while AVG ranks lowest in terms of accuracy.

Table 4 summarizes the runtimes for all friction models across different resolutions. As observed in the previous test case, AVG, CFS, and PFA demonstrate similar time costs, whereas PFE incurs a

60%–80% additional time burden due to the computational demands of friction calculations on the high-resolution mesh. Based on the combined evaluation of time cost and accuracy, PFA emerges as the model that strikes the best balance between these two factors.

Test Case 3: Red River Flood Event

This test case aims to evaluate the performance of the friction upscaling methods in simulating a real-world flood inundation scenario. The test replicates a severe flood event that occurred on the Red River over a 7-day period starting from May 4, 2022. Originating at the confluence of the Bois de Sioux and Otter Tail rivers between the U.S. states of Minnesota and North Dakota, the Red River flows northward through the Red River Valley before reaching Lake Winnipeg. With a gentle slope (about 0.01% - 0.02%), the Red River spans 885 kilometers in length, with approximately two-thirds of its length in the United States and the remainder in Canada (Minnesota Department of Natural Resources 2019).

The computational domain for this study covers an area extending 24 kilometers east and west, and 60 kilometers north and south, as illustrated in Fig. 7. The domain includes a primary reach from south to north, marked in blue, along with several tributaries (indicated in beige) that join the main reach. Along the domain edge, a closed boundary condition is set except for the 10 points shown in Fig. 7, where inflow/outflow boundary conditions (BC) are applied. All BCs introduce inflow, except for BC 9, located at the northern extent of the domain, which acts as an outflow point. The applied boundary conditions for BCs are provided in Fig. 8. The initial condition is derived from the outcomes of a steady-state flow simulation using the flow characteristics at t=0 s. The distribution of Manning roughness is inferred from the land cover maps, as illustrated in Fig. 9. High-resolution gridded topographic data at 5 m resolution, as shown in Fig. 10, is used as the base mesh for the computational meshes at resolutions of 200, 300, 400, 500, and 600 m to establish the friction upscaling methods in the SG model. In this test case, the performance of the models at different resolutions is evaluated against BMS (50).

Fig. 11 displays the time series of water surface levels at two distinct points, P1 and P2, located respectively in the floodplain and main channel of the Red River, at the points depicted in Fig. 10.

While solutions were successful across all models and resolutions, for clarity, only the results of the BMS (50), along with the highest and lowest mesh solutions for all friction models, are depicted. The results indicate that resolution plays a more critical role than the specific upscaling method used, with higher resolution meshes yielding solutions closer to the BMS (50). This is likely due to the impact of resolution on the approximation of various terms in the equations, beyond just friction. Notably, the AVG model demonstrates the poorest accuracy among all solutions, exhibiting a substantial underestimation of depths. For example, the difference between AVG (600/5) and CFS (600/5) at $t = 168$ hr is approximately 0.4 m and 0.2 m at points P1 and P2, respectively. Except for AVG, prior to $t = 40$ hr, other solutions at the presented mesh resolutions tend to overestimate the free-surface elevation, followed by underestimation for the remainder of the simulation. In terms of accuracy, the models can be ranked as follows: PFE, PFA, CFS, and AVG.

Fig. 12 provides a conventional analysis of model convergence (adapted here to the problem of dual-mesh modeling) through a log-log graph illustrating the RMSE of model solutions as a function of the resolution of the coarse mesh. This analysis focuses on $t = 168$ hr, i.e. at the end of the simulation at the peak inundation within the domain. Each model solution at every resolution is post-processed to obtain water depth consistent with a 5 m resolution, facilitating comparison with the benchmark model solution [i.e., BMS (50)]. The graph reveals consistent patterns among the RMSE of model solutions across all models, which display approximately parallel trends. The RMSE range for CFS, PFA, and PFE is notably narrow, differing by only a few centimeters. However, for AVG, this difference is more pronounced. For instance, at resolutions of 200 m and 600 m, the RMSE for CFS, PFA, and PFE ranges between 0.05-0.07 m and 0.24-0.29 m, respectively, whereas for AVG, it nearly doubles to 0.105 m and 0.39 m at the same resolutions. Among CFS, PFA, and PFE, PFE exhibits the most accurate solutions, followed by PFA and then CFS.

Table 5 examines the computational cost and speedup relative to BMS (50) for all the simulations. The table reveals that PFE, which upscales the friction source term at high-resolution mesh scales during the simulation, exhibits a 2-5 times slower performance compared to CFS, PFA, and AVG.

This is because AVG performs computations at low-resolution mesh and CFS and PFA transfer a significant portion of computations to pre-processing. Increasing the $\Delta X/\delta x$ ratio (i.e., a larger number of small cells within each computational cell) reduces the speedup achieved by PFE but has minimal impact on the performance of the other friction models. For more details on the effects of $\Delta X/\delta x$ on model performance, see Shamkhalchian 2021 and Shamkhalchian and de Almeida 2021. Fig. 13 provides additional insights into the efficiency of the different approaches. In Fig. 13a, the variation of the time cost C against the mesh resolution is illustrated in a log-log graph. As discussed in the introduction, the relationship between time cost and computational resolution follows $C \sim \Delta x^{-P}$, where $P = 3$ for single mesh explicit models. In the case of AVG, CFS, and PFA, $P = 2.2$, while for PFE, $P = 1.5$. The values of P less than 3 for the SG model primarily stem from the computation of fluxes at small cell resolutions along the cell edges (Shamkhalchian and de Almeida 2021; Shamkhalchian and de Almeida 2023). Fig. 13b directly examines the trade-off between computational performance and accuracy, enabling a comparison of the efficiency among the tested models. In this figure, the model results at the left-low corner are the best performers, delivering the most accurate solutions at a given computational time (or vice-versa). For instance, if targeting a simulation with a time cost of 20 hr, the models AVG, CFS, PFA, and PFE yield RMSE values of approximately 0.16, 0.11, 0.1, and 0.27 m respectively.

An analysis of flood extension analysis was conducted for different solutions. No meaningful differences were detected between the solutions at different resolutions, which may reside in topographic features of the domain of study. In Fig. 14, for the sake of conciseness and clarification the maps based on the solutions BMS (50), AVG (600/5), and PFA (600/5) are presented.

DISCUSSION AND CONCLUSION

This research comparatively investigates methods proposed in the literature to approximate the friction source term of the 2D SWE in computational simulations using nested mesh models for large-scale flood inundation problems. To achieve this objective, the second-order accuracy SG model by Shamkhalchian and de Almeida 2023 is used. The SG model comprises coarse Cartesian computational meshes hosting fine Cartesian meshes that represent high-resolution topographic

and roughness data. To improve accuracy, a FV methodology has been developed to solve the governing equations at the fine mesh level and then upscale the solution for the coarse mesh. This approach aims to shift a significant portion of the computational burden to the pre-processing stage for efficiency purposes.

Four specific approaches are investigated in this study to approximate friction, each based on different assumptions and methodologies as follows. (1) AVG, which utilizes averaged values of computational cells to approximate the friction source term. (2) CFS, whereby computations are performed at the high-resolution mesh using the methodology proposed by Sanders and Schubert 2019. In this model, a portion of the computational cost is shifted to pre-processing, thereby improving the model's efficiency. The main assumption in this model is that the friction slope remains constant within a large cell. While assuming a constant friction slope ($\mathbf{S}_f$) to approximate the distribution of flow at given cross-sections has been the subject of previous examination and is widely used (e.g., Hec-Ras), extending this idea to assume that $\mathbf{S}_f$ is constant over an area of flow is questionable and warrants further examination. For example, let us consider a hypothetical scenario of a 1D prismatic rectangular channel over irregular bed topography under steady-state flow. Assuming a constant value of Manning's coefficient n_M along the channel for simplicity, if both discharge ($\mathbf{q}$) and $\mathbf{S}_f$ are assumed constant ($\mathbf{q}$ = constant since the flow is steady), it would imply that the water depth (h) should also be constant along the channel. This contradicts the very assumption of a horizontal water surface over varied topography, which forms the basis of most models in approximating the friction source term. In general, assuming a constant value of $\mathbf{S}_f$ over a large computational area seems inaccurate, as the friction slope may significantly change due to the acceleration of flow induced by fine-resolution topography. (3) PFE, proposed by Shamkhalchian and de Almeida 2021 and Shamkhalchian and de Almeida 2023, was formulated in a bid to overcome the unrealistic assumption of a constant friction slope over a large computational cell. The method did not assume constant values of variables within the large cell, but instead introduced the simplifying assumption that the flow direction remains constant within a large cell. This approach is implemented at the high-resolution mesh level (i.e. friction estimated for each

small cell), which is computationally expensive. (4) PFA was developed by Shamkhalchian and de Almeida 2021 and Shamkhalchian and de Almeida 2023 to reduce the computational cost of PFE by approximating the solution of PFE using an innovative methodology that offloads many computations to the pre-processing stage. This enables the model to approximate the friction source term at the level of computational cells.

All four models are evaluated using both idealized and real-world test cases. The results from these simulations indicate that AVG, CFS, and PFA have similar efficiency and are 2-5 times faster than PFE. Unlike PFE, which performs all computations during the simulation, AVG, CFS, and PFA can shift part of the computational load to preprocessing or handle it at larger cell scales. However, the accuracy of AVG is notably degraded at coarse mesh resolutions compared to the other three models. Our results indicate that PFA may represent an optimal balance between accuracy and speedup, making it the most suitable choice overall for practical applications. Nevertheless, the degree of accuracy can vary depending on specific test case characteristics. For instance, while AVG generally yields lower accuracy at low-resolution meshes, in scenarios with minimal bed level and roughness variation, its accuracy can be comparable to that of the other models.

DATA AVAILABILITY STATEMENT

All data that support the findings of this study are available from the corresponding author upon reasonable request.

ACKNOWLEDGEMENTS

The authors extend their gratitude to the University of Manitoba for granting access to data storage and the high-performance computing system, Grex, which served as the foundation for the simulations conducted in this paper. Special thanks are also due to the Ministry of Transportation and Infrastructure in Manitoba (MTI), specifically The Hydrologic Forecast Centre (HFC), for generously providing the hydrological, topographic, and land cover data essential for the real-world test case used in this study.

SUPPLEMENTAL MATERIALS

Figures S1–S3 and Table S1 are available online in the ASCE Library (www.ascelibrary.org).

NOTATION

The following symbols are used in this paper:

C = computational cost, runtime and time cost (s or h);

$\mathbf{e}$ = unit outward vector normal to cells boundary (-, -);

e_x, e_y = x and y components of $\mathbf{e}$ (-);

E = flux tensor ($\mathrm{m^2\ s^{-1}},\ \mathrm{m^3\ s^{-2}}, \mathrm{m^3\ s^{-2}}$ | $\mathrm{m^2\ s^{-1}},\ \mathrm{m^3\ s^{-2}}, \mathrm{m^3\ s^{-2}}$);

$\mathbf{E}'$ = numerical flux vector ($\mathrm{m^2\ s^{-1}}$, $\mathrm{m^3\ s^{-2}}$, $\mathrm{m^3\ s^{-2}}$);

$\mathbf{F}, \mathbf{G}$ = flux vectors in the x and y directions ($\mathrm{m^2\ s^{-1}},\ \mathrm{m^3\ s^{-2}},\ \mathrm{m^3\ s^{-2}}$);

g = acceleration due to gravity ($\mathrm{m\ s^{-2}}$);

h = water depth (m);

J, K = number of columns and rows of the small cells in a large cell (-);

L_d = length of the study domain (m);

n = time level ($\mathrm{s\ m^{-1/3}}$);

n_M = Manning coefficient (-);

N = number of computational cells (-);

N_w = number of submerged small cells in a large cell (-);

N_Γ = number of submerged small cells adjacent to the cell boundary (-);

$q_x,\ q_y$ = x and y components of unit width discharge ($\mathrm{m^2\ s^{-1}}$);

$\mathbf{q}$ = vector of unit width discharge ($\mathrm{m^2\ s^{-1}}$);

Q = flow discharge ($\mathrm{m^3\ s^{-1}}$);

r = ratio between the wet area and the whole area of a large cell (-);

S_{0_x}, S_{0_y} = x and y components of bed slope (-);

S_{f_x}, S_{f_y} = x and y components of frictional slope (-);

$\mathbf{S}$ = vector of source terms ($\mathrm{m\ s^{-1}}$, $\mathrm{m^2\ s^{-2}}$, $\mathrm{m^2\ s^{-2}}$);

$\mathbf{S}_b$ = vector of bed slope source term (m s^{-1}, m^2 s^{-2}, m^2 s^{-2});

$\mathbf{S}_f$ = vector of frictional slope (−,−);

$\mathbf{S}_r$ = vector of friction slope source term (m s^{-1}, m^2 s^{-2}, m^2 s^{-2});

t = time (s or hr);

T_p = parameters in Eq. 12, $p = 1, 2, 3$ $\left(\text{m}^{(p-2/3)}\ \text{s}^{-1}\right)$;

T_p = parameters in Eq. 30, $p = 4, 5, 6$ $\left(\text{m}^{(p-10/3)}\ \text{s}^{-2}\right)$;

u, v = x and y velocity components (m s^{-1});

$\mathbf{U}$ = flow variable vector (m, m^2 s^{-1}, m^2 s^{-1});

U^+ = flow variable vector of the neighboring cell (m, m^2 s^{-1}, m^2 s^{-1});

$\mathbf{V}$ = velocity vector (m s^{-1}, m s^{-1});

W_d = width of the study domain (m);

x, y = Cartesian coordinates (m);

z = bed level (m);

$\acute{z}$ = a binary elevation function giving the minimum of bed and water surface level (m);

Γ = boundary length (m);

$\Gamma_1 - \Gamma_4$ = four edges of a large cell as defined in Fig. 1 (-);

$\delta x, \delta y$ = dimensions of small cells (m);

$\Delta X, \Delta Y$ = dimensions of large cells (m);

Δt = time step (s);

η = water surface elevation (m);

σ = frictional correction coefficient of intermediate state unit width discharge (-);

φ = coefficient of unit width discharge distribution (-);

ψ_a = approximated cross-section's conveyance (m^2 s^{-1});

Ω = cell area (m^2);

Ω_w = wet area of a cell (m^2);

REFERENCES

Alcrudo, F. and García-Navarro, P. (1993). "A high-resolution godunov-type scheme in finite volumes for the 2d shallow-water equations." *International Journal for Numerical Methods in Fluids*, 16(6), 489–505.

Begnudelli, L., Sanders, B. F., and Bradford, S. F. (2008). "Adaptive godunov-based model for flood simulation." *Journal of Hydraulic Engineering*, 134(6), 714–725.

Bermudez, A. and Vazquez, M. E. (1994). "Upwind methods for hyperbolic conservation laws with source terms." *Computers & Fluids*, 23(8), 1049–1071.

Burguete, J., García-Navarro, P., Murillo, J., and García-Palacín, I. (2007). "Analysis of the friction term in the one-dimensional shallow-water model." *Journal of Hydraulic Engineering*, 133(9), 1048–1063.

Cea, L. and Bladé, E. (2015). "A simple and efficient unstructured finite volume scheme for solving the shallow water equations in overland flow applications." *Water resources research*, 51(7), 5464–5486.

Chow, V. T. (1959). *Open channel hydraulics*. McGraw-Hill.

Cunge, J. A., Holly, F. M., and Verwey, A. (1980). *Practical aspects of computational river hydraulics*. Pitman Publishing Ltd.

de Almeida, G. A., Bates, P., and Ozdemir, H. (2018). "Modelling urban floods at submetre resolution: challenges or opportunities for flood risk management?." *Journal of Flood Risk Management*, 11, S855–S865.

Defina, A., D'Alpaos, L., and Matticchio, B. (1994). "A new set of equations for very shallow water and partially dry areas suitable to 2D numerical models." *Modelling of flood propagation over initially dry areas*, ASCE, 72–81.

Dewals, B., Bruwier, M., Pirotton, M., Erpicum, S., and Archambeau, P. (2021). "Porosity models for large-scale urban flood modelling: A review." *Water*, 13(7), 960.

Duran, A. and Marche, F. (2014). "Recent advances on the discontinuous Galerkin method for shallow water equations with topography source terms." *Computers & Fluids*, 101, 88–104.

Erduran, K., Kutija, V., and Hewett, C. (2002). "Performance of finite volume solutions to the

shallow water equations with shock-capturing schemes." *International journal for numerical methods in fluids*, 40(10), 1237–1273.

Guinot, V., Sanders, B. F., and Schubert, J. E. (2017). "Dual integral porosity shallow water model for urban flood modelling." *Advances in water resources*, 103, 16–31.

Guinot, V. and Soares-Frazão, S. (2006). "Flux and source term discretization in two-dimensional shallow water models with porosity on unstructured grids." *International Journal for Numerical Methods in Fluids*, 50(3), 309–345.

Horritt, M. and Bates, P. (2001). "Effects of spatial resolution on a raster based model of flood flow." *Journal of Hydrology*, 253(1), 239–249.

Horváth, Z., Buttinger-Kreuzhuber, A., Konev, A., Cornel, D., Komma, J., Blöschl, G., and ... Waser, J. (2020). "Comparison of fast shallow-water schemes on real-world floods." *Journal of Hydraulic Engineering*, 146(1), 05019005.

Hénonin, J., Hongtao, M. A., Zheng-Yu, Y., Hartnack, J., Havnø, K., Gourbesville, P., and Mark, O. (2015). "Citywide multi-grid urban flood modelling: the July 2012 flood in Beijing." *Urban Water Journal*, 12(1), 52–66.

Kang, Y. and Kubatko, E. J. (2024). "An automatic mesh generator for coupled 1d–2d hydrodynamic models." *Geoscientific Model Development*, 17(4), 1603–1625.

Kesserwani, G. and Liang, Q. (2012). "Locally limited and fully conserved RKDG2 shallow water solutions with wetting and drying." *Journal of scientific computing*, 50(1), 120–144.

Kesserwani, G. and Liang, Q. (2015). "RKDG2 shallow-water solver on non-uniform grids with local time steps: Application to 1D and 2D hydrodynamics." *Applied Mathematical Modelling*, 39(3-4), 1317–1340.

Kesserwani, G. and Sharifian, M. K. (2023). "(Multi) wavelet-based godunov-type simulators of flood inundation: Static versus dynamic adaptivity." *Advances in Water Resources*, 171, 104357.

Kirstetter, G., Delestre, O., Lagrée, P.-Y., Popinet, S., and Josserand, C. (2021). "B-flood 1.0: an open-source saint-venant model for flash-flood simulation using adaptive refinement." *Geoscientific Model Development*, 14(11), 7117–7132.

Kong, C. (2011). "Comparison of approximate Riemann solvers." M.S. thesis, Department of dvmv,University of Reading, Reading, UK, Department of dvmv,University of Reading, Reading, UK.

LeVeque, R. J. (2002). *Finite volume methods for hyperbolic problems*. Cambridge University Press.

Liang, Q. and Marche, F. (2009). "Numerical resolution of well-balanced shallow water equations with complex source terms." *Advances in water resources*, 32(6), 873–884.

Lions, P. L. and Mercier, B. (1979). "Splitting algorithms for the sum of two nonlinear operators." *SIAM Journal on Numerical Analysis*, 16(6), 964–979.

MacDonald, I. (1996). "Analysis and computation of steady open channel flow." Ph.D. thesis, University of Reading, Reading, UK, University of Reading, Reading, UK.

Minnesota Department of Natural Resources (2019). "Red river of the north state water trail. Retrieved from https://www.dnr.state.mn.us/watertrails/redriver/index.html.

Morales-Hernández, M., Petaccia, G., Brufau, P., and García-Navarro, P. (2016). "Conservative 1D–2D coupled numerical strategies applied to river flooding: The Tiber (Rome)." *Applied Mathematical Modelling*, 40(3), 2087–2105.

Neal, J., Fewtrell, T., and Trigg, M. (2009). "Parallelisation of storage cell flood models using OpenMP." *Environmental Modelling & Software*, 24(7), 872–877.

Qi, X., de Almeida, G. A., and Maldonado, S. (2024). "Physics-informed neural networks for solving flow problems modeled by the 2d shallow water equations without labeled data." *Journal of Hydrology*, 636, 131263.

Rogers, B., Fujihara, M., and Borthwick, A. G. (2001). "Adaptive Q-tree Godunov-type scheme for shallow water equations." *International Journal for Numerical Methods in Fluids*, 35(3), 247–280.

Sanders, B. F. and Schubert, J. E. (2019). "Primo: Parallel raster inundation model." *Advances in Water Resources*, 126, 79–95.

Sanders, B. F., Schubert, J. E., and Gallegos, H. A. (2008). "Integral formulation of shallow-water equations with anisotropic porosity for urban flood modeling." *Journal of hydrology*, 362(1-2),

19–38.

Shamkhalchian, A. (2021). “High-performance numerical models for large scale flood inundation problems.” Ph.D. thesis, Department of Civil, Maritime & Environmental Engineering, University of Southampton, Department of Civil, Maritime & Environmental Engineering, University of Southampton.

Shamkhalchian, A. and de Almeida, G. A. M. (2021). “Upscaling the shallow water equations for fast flood modelling.” *Journal of Hydraulic Research*, 59(5), 739–756.

Shamkhalchian, A. and de Almeida, G. A. M. (2023). “Effects of reconstruction of variables on the accuracy and computational performance of upscaling solutions of the shallow water equations.” *Journal of Hydraulic Research*, 1–13.

Shaw, J. and Kesserwani, G. (2020). “Stochastic Galerkin finite volume shallow flow model: well-balanced treatment over uncertain topography.” *Journal of Hydraulic Engineering*, 146(3), 04020005.

Soares-Frazão, S., Lhomme, J., Guinot, V., and Zech, Y. (2008). “Two-dimensional shallow-water model with porosity for urban flood modelling.” *Journal of Hydraulic Research*, 46(1), 45–64.

Toro, E. F. (2001). *Shock-capturing methods for free-surface shallow flows*. John Wiley.

Toro, E. F. (2013). *Riemann solvers and numerical methods for fluid dynamics: a practical introduction*. Springer Science & Business Media.

Toro, E. F. and Garcia-Navarro, P. (2007). “Godunov-type methods for free-surface shallow flows: A review.” *International Journal for Numerical Methods in Fluids*, 45(6), 736–751.

Toro, E. F., Spruce, M., and Speares, W. (1994). “Restoration of the contact surface in the HLL-Riemann solver.” *Shock waves*, 4(1), 25–34.

Valiani, A. and Begnudelli, L. (2006). “Divergence form for bed slope source term in shallow water equations.” *Journal of Hydraulic Engineering*, 132(7), 652–665.

Viero, D. P. and Valipour, M. (2017). “Modeling anisotropy in free-surface overland and shallow inundation flows.” *Advances in Water Resources*, 104, 1–14.

Volp, N., Van Prooijen, B., and Stelling, G. (2013). “A finite volume approach for shallow water

668 flow accounting for high-resolution bathymetry and roughness data." *Water Resources Research*,
669 49(7), 4126–4135.
670 Wang, Y., Liang, Q., Kesserwani, G., and Hall, J. W. (2011). "A positivity-preserving zero-inertia
671 model for flood simulation." *Computers Fluids*, 46(1), 505–511 10th ICFD Conference Series
672 on Numerical Methods for Fluid Dynamics (ICFD 2010).
673 Wijaya, O. T., Yang, T. H., Hsu, H. M., and Gourbesville, P. (2023). "A rapid flood inundation
674 model for urban flood analyses." *MethodsX*, 10, 102202.
675 Xing, Y., Chen, H., Liang, Q., and Ma, X. (2022). "Improving the performance of city-scale
676 hydrodynamic flood modelling through a GIS-based DEM correction method." *Natural Hazards*,
677 112(3), 2313–2335.
678 Yin, Z., Shi, J., Bian, L., Campbell, W. H., Zanje, S. R., Hu, B., and Leon, A. S. (2025).
679 "Physics-informed neural network approach for solving the one-dimensional unsteady shallow-
680 water equations in riverine systems." *Journal of Hydraulic Engineering*, 151(1), 04024060.
681 Yu, D. and Lane, S. N. (2006). "Urban fluvial flood modelling using a two-dimensional diffusion-
682 wave treatment, part 2: development of a sub-grid-scale treatment." *Hydrological Processes*,
683 20(7), 1567–1583.

List of Tables

TABLE 1. Range of Variability in RMSE for the Models (m) in Test Case 1. The results represent the analysis of errors observed at each resolution of every model in comparison to the Benchmark Solutions (BMS) on days 2, 5, 7, 9, and 13.

Cell Zize	Range of RMSE for the Models (m)			
(m)	AVG	CFS	PFA	PFE
100/1	0.191-0.295	0.031-0.038	0.018-0.022	0.016-0.021
200/1	0.194-0.293	0.032-0.046	0.020-0.026	0.020-0.025
300/1	0.196-0.296	0.039-0.051	0.026-0.033	0.026-0.031

TABLE 2. Runtimes of the models for the Test Case 1.

Cell Zize	Runtime of Models (s)			
(m)	AVG	CFS	PFA	PFE
100/1	258	291	287	751
200/1	230	238	238	679
300/1	180	190	188	737

TABLE 3. RMSE of water surface elevation for the models, compared to the analytical solution at the center of computational cells, across various mesh resolutions in Test Case 2.

Cell Zize	Range of RMSE for the Models (m)			
(m)	AVG	CFS	PFA	PFE
100/1	0.575	0.485	0.472	0.457
200/1	0.583	0.496	0.484	0.469
300/1	0.597	0.517	0.507	0.492

TABLE 4. Runtimes of the models for the Test Case 2.

Cell Zize	Runtime of Models (s)			
(m)	AVG	CFS	PFA	PFE
100/1	22.00	22.42	22.60	37.01
200/1	19.02	20.10	19.71	34.50
300/1	17.02	16.80	17.66	30.03

TABLE 5. Time costs (C) of model solutions at various resolutions for the real-world test case.

Solution	C (hr)	Speedup
AVG (200/5)	36.4	2.7
AVG (300/5)	13.9	7
AVG (400/5)	8	12.2
AVG (500/5)	5	19.4
AVG (600/5)	3.3	29.6
BMS (50/)	97	1
CFS (200/5)	33	2.9
CFS (300/5)	14	6.9
CFS (400/5)	7.9	12.3
CFS (500/5)	4.9	19.8
CFS (600/5)	3	32.3
PFA (200/5)	34.4	2.8
PFA (300/5)	13.7	7.1
PFA (400/5)	7.9	12.3
PFA (500/5)	4.8	20.2
PFA (600/5)	3.1	31.3
PFE (200/5)	83.7	1.2
PFE (300/5)	44.8	2.2
PFE (400/5)	28.7	3.4
PFE (500/5)	22.1	4.4
PFE (600/5)	15.9	6.1

List of Figures

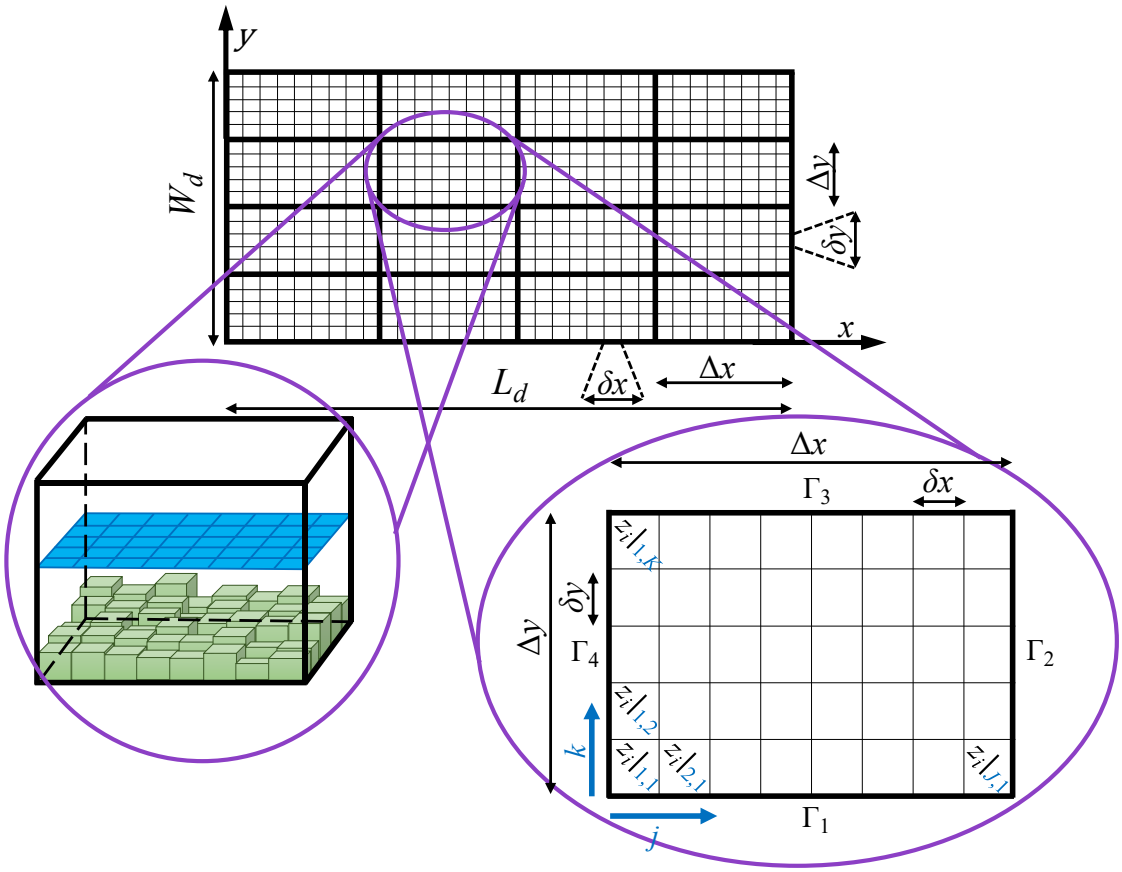

Fig. 1. Structure and symbols used to describe the nested meshes in the SG model

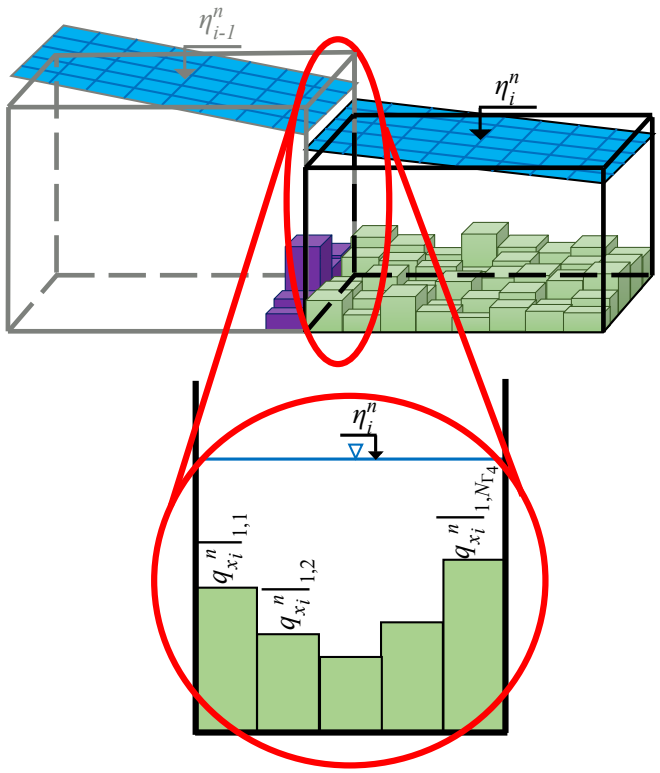

Fig. 2. Redistributing averaged variable values at edge Γ_4 of a large cell to reconstruct Riemann problem states at the high-resolution mesh.

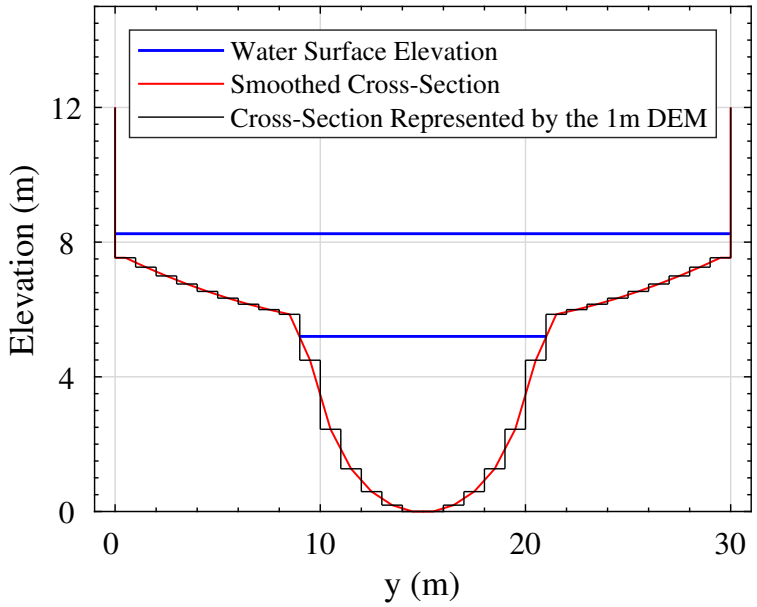

Fig. 3. Cross-section for the Test case 1. While the actual geometry of the cross-section is smooth, the 1-meter DEM represents it as a piecewise constant.

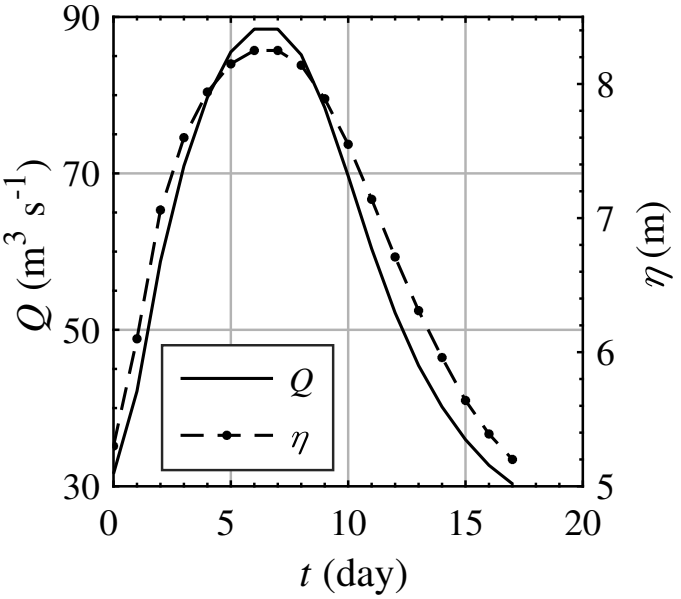

Fig. 4. Time series of upstream discharge *Q(t)* and downstream water surface elevation $\eta(t)$ used as boundary conditions in Test 1.

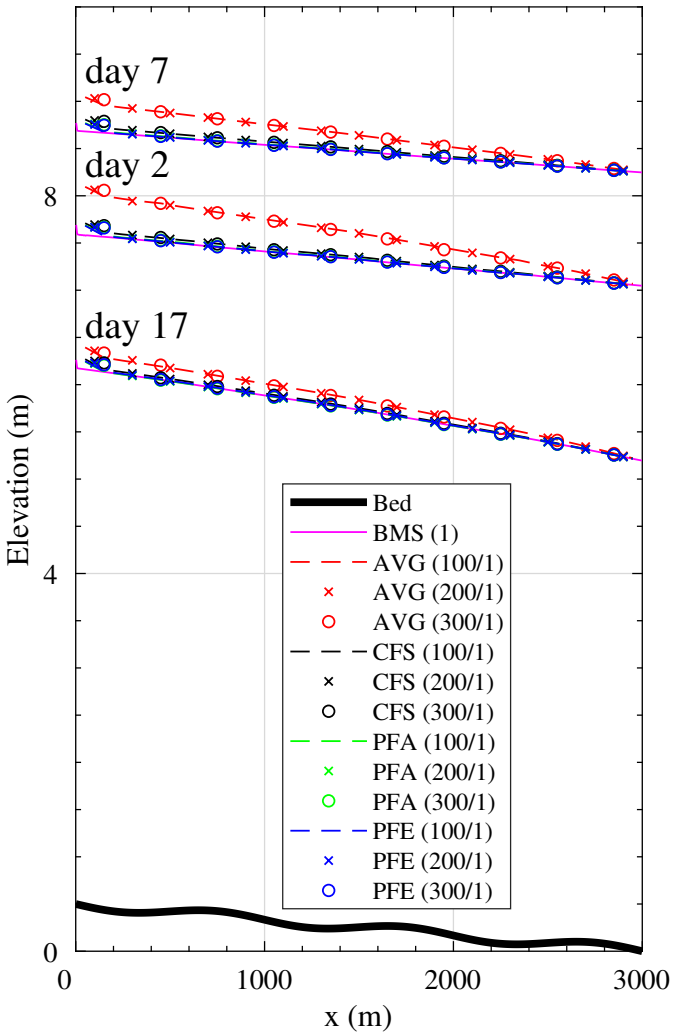

Fig. 5. Longitudinal profile of the models at various resolutions. For clarity, only the results at t=2, 7, and 17 days are depicted.

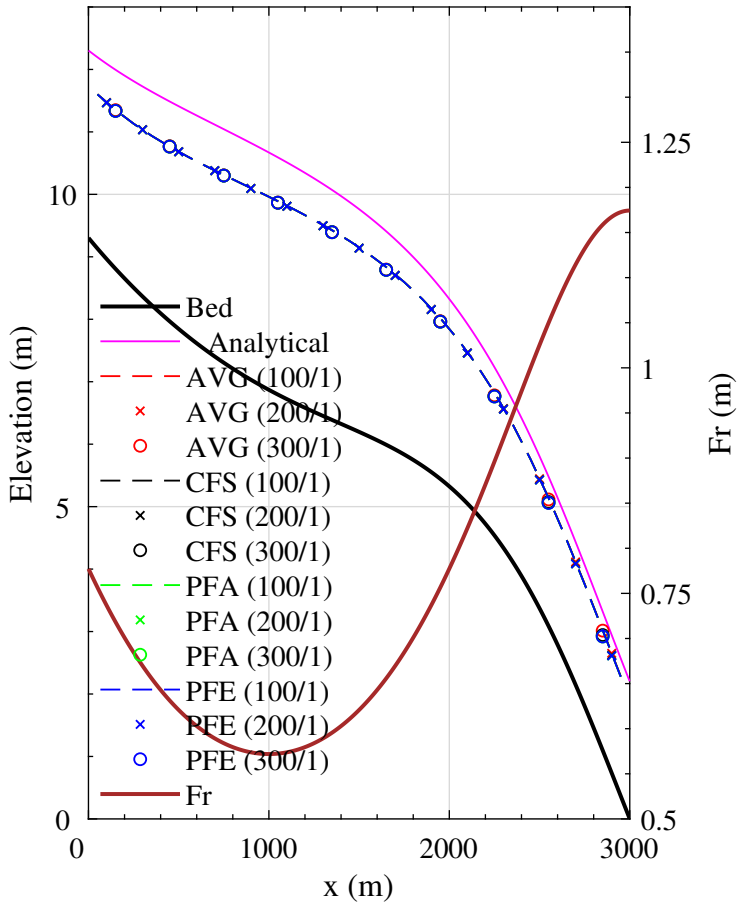

Fig. 6. Longitudinal profiles of the Froude number and solutions at different resolutions for Test Case 2.

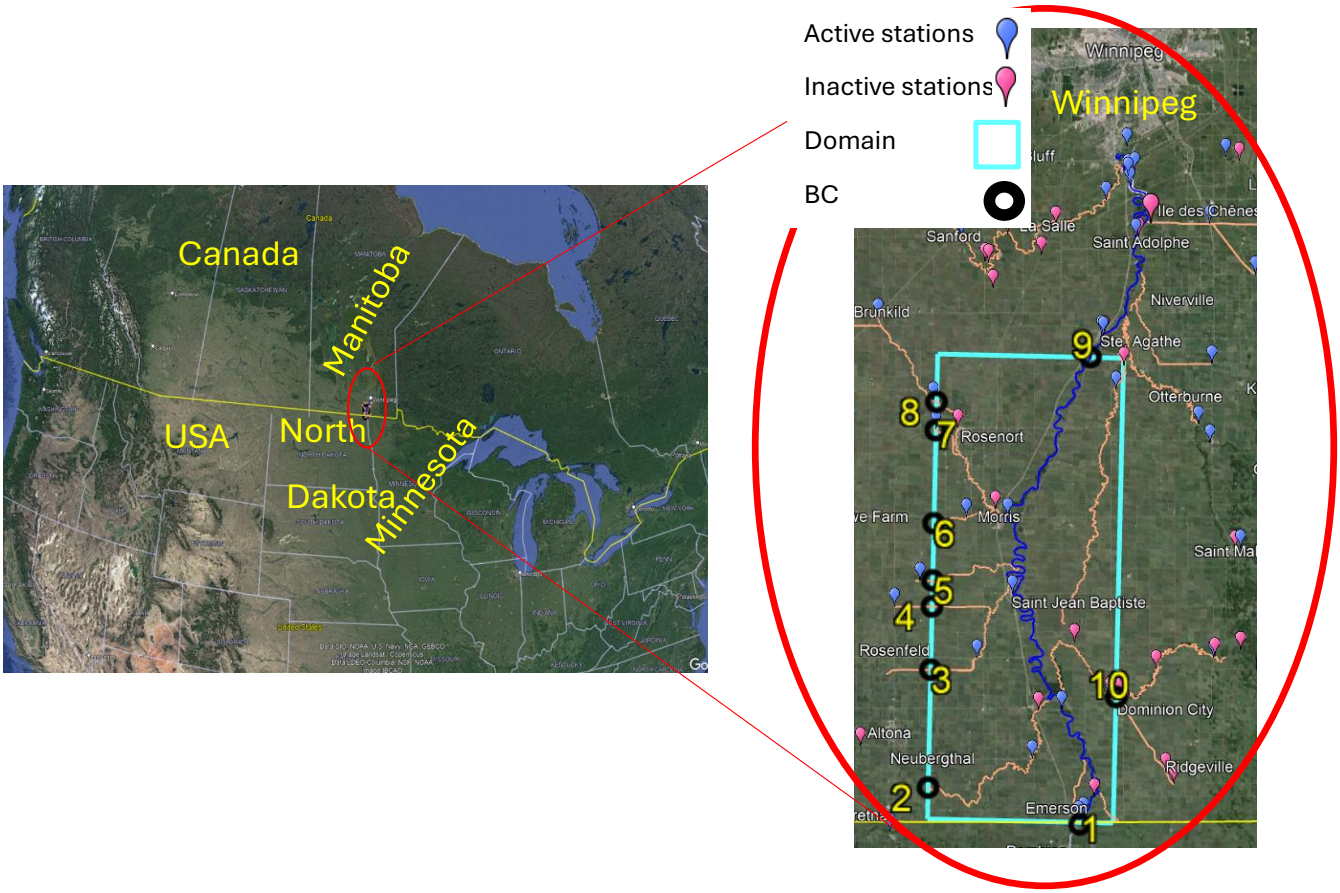

Fig. 7. Computational domain for Red River Flood Study.

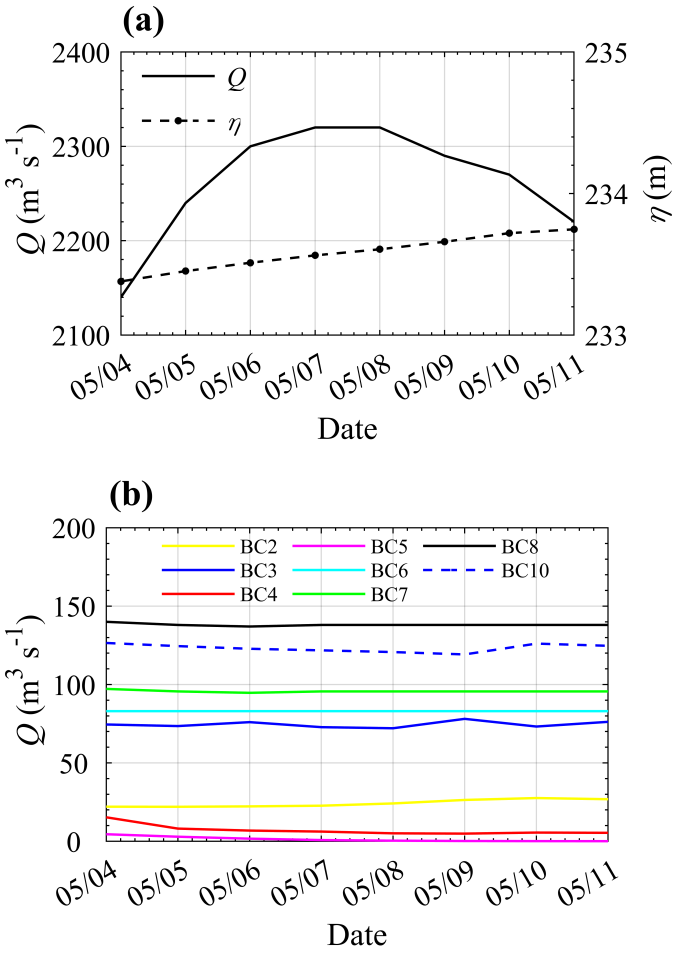

Fig. 8. Boundary conditions applied to the BCs: (a) Time series of discharge and water surface elevation for BC1 and BC9, respectively. (b) Discharge hydrograph for the remaining BCs.

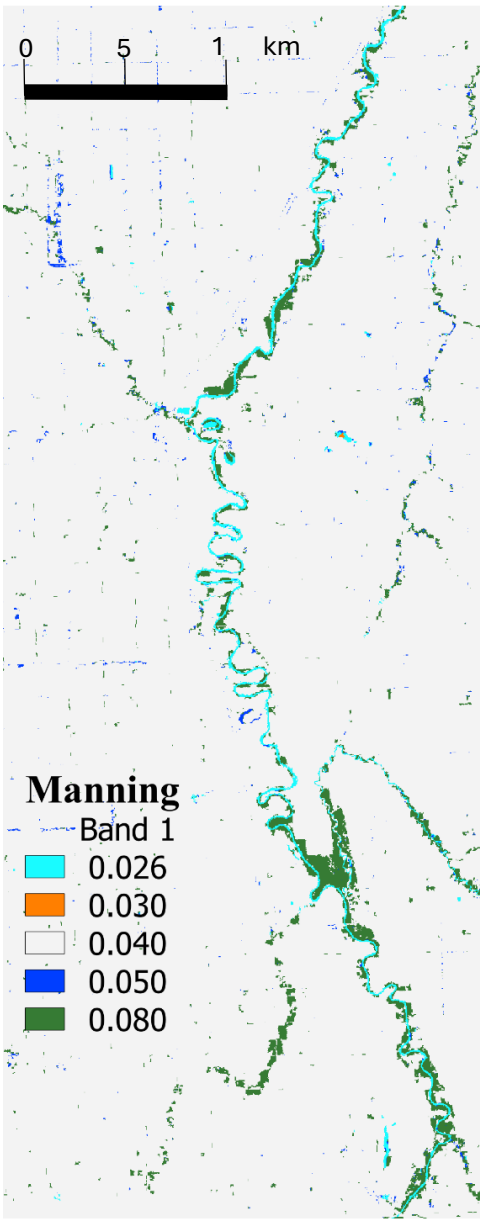

Fig. 9. Map illustrating the spatial distribution of Manning roughness coefficients across the study area for the real-world test scenario.

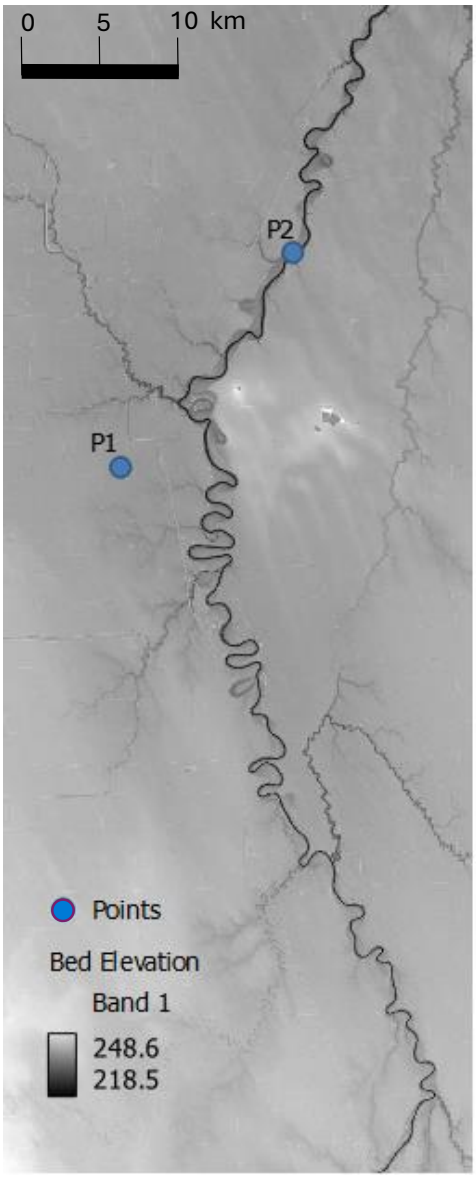

Fig. 10. Topography employed for Test Case 2 at a resolution of 5m. Points P1 and P2, located on the main channel and floodplain respectively, are utilized for comparing results obtained by the friction models previously introduced.

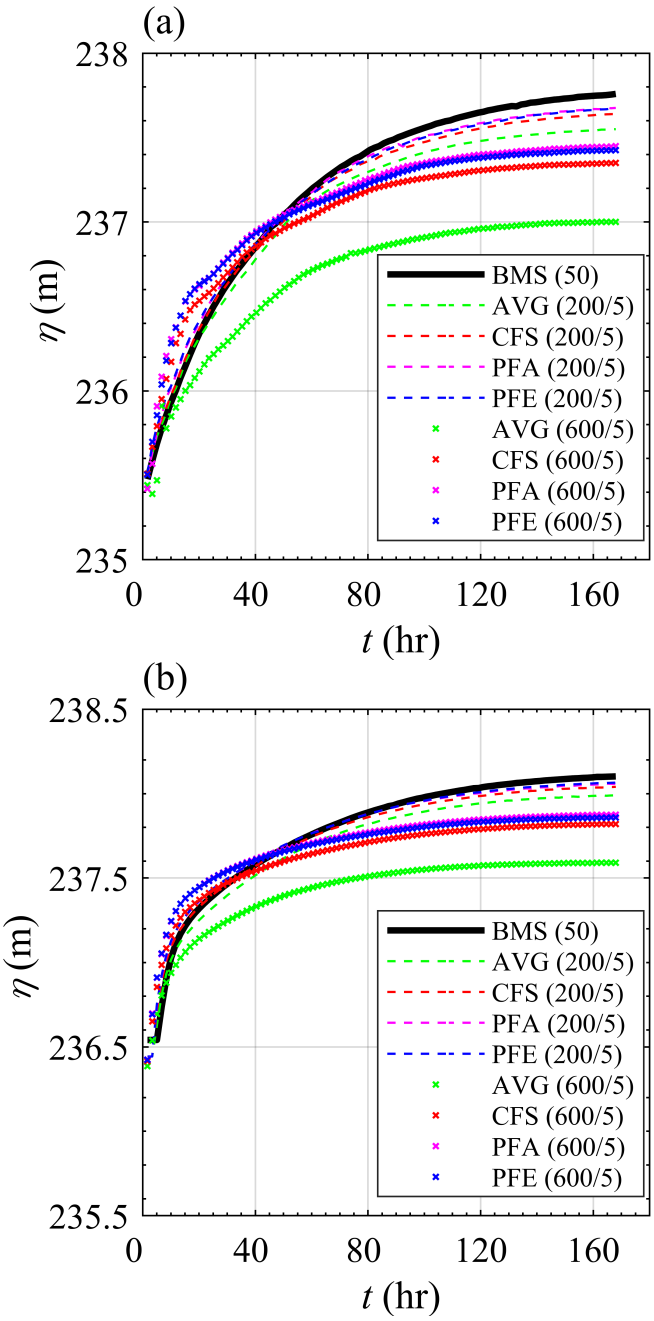

Fig. 11. Time series of water surface elevation solutions at points (a) P1 on the floodplain, and (b) P2, in the main channel of the river. Computational cells at the highest and lowest resolutions compared against the BMS (50) are shown for clarity.

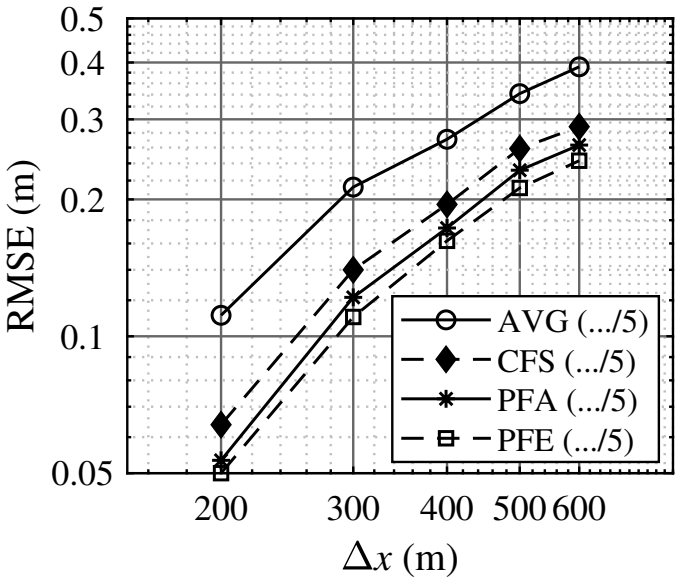

Fig. 12. Comparison of predicted water depth RMSE

at various resolutions relative to benchmark results at the end of simulation t = 168), with maximum inundation within the study domain observed in the real-world test case.

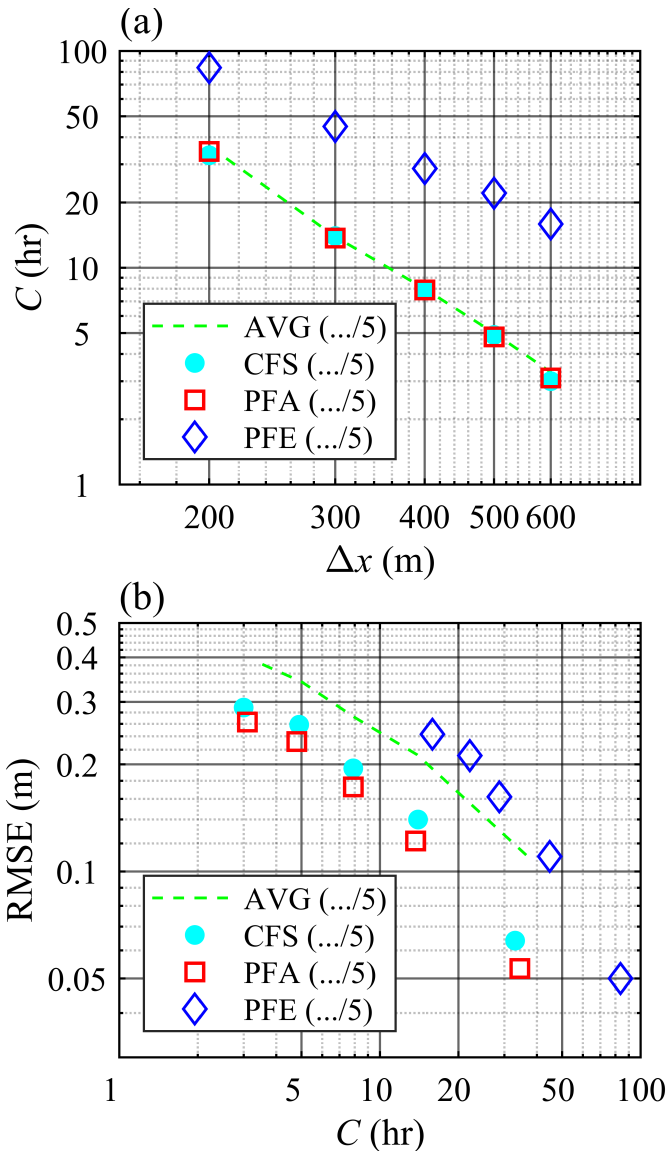

Fig. 13. (a) Comparison of time costs (C) for various model solutions at different computational resolutions, and (b) Relationship between the variation in water depth RMSE of model solutions, relative to the benchmark solution at the end of the simulation (t = 168 hr), and their corresponding time costs for the real-world test case.

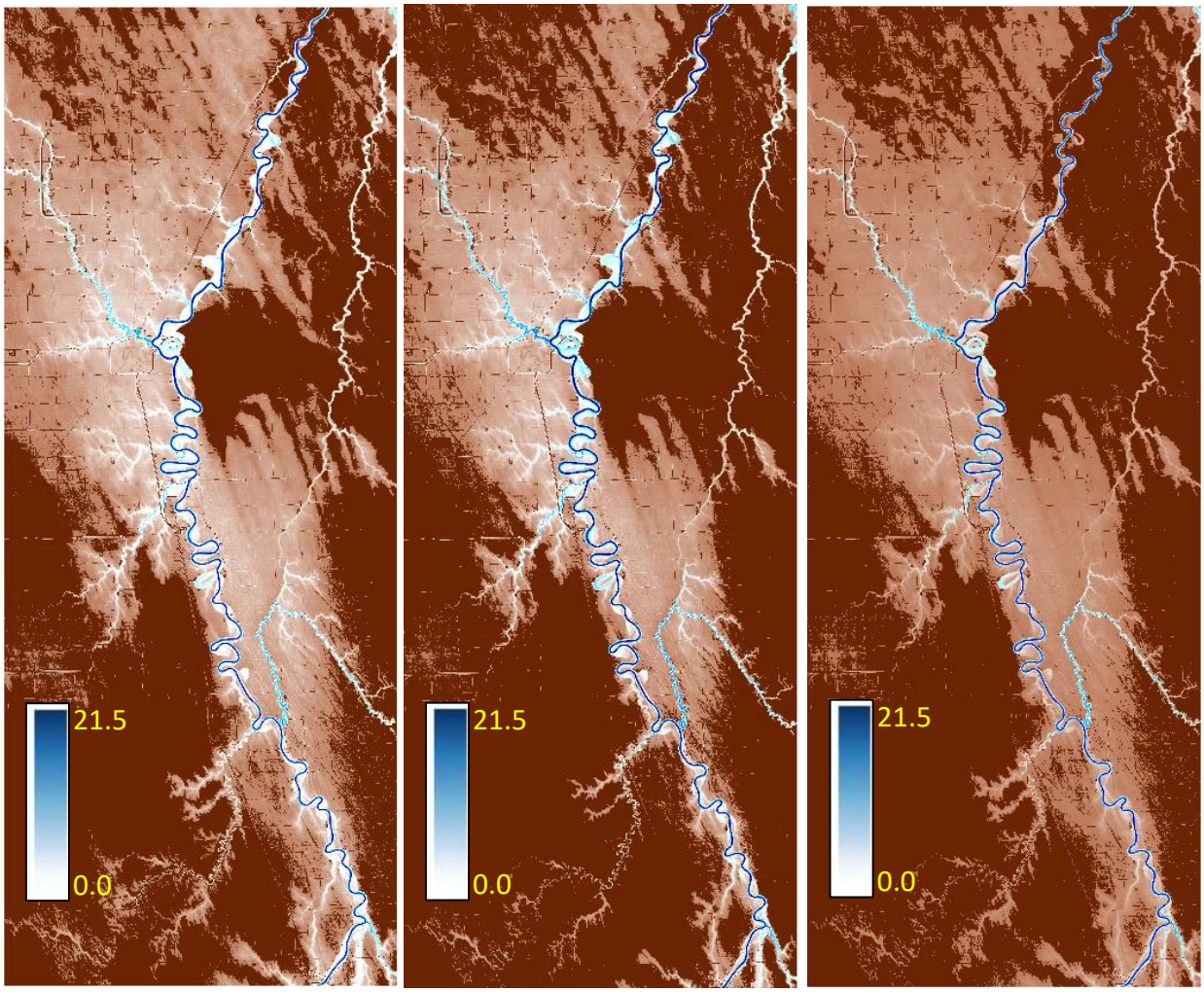

Fig. 14. Flood extent in the study domain for different solutions at $t = 168$ hr, with water depth ranging from 0 to 21.5 m.